Soft impurity walls and hard-wall branch promotion in a superconducting two-dimensional SSH model

Henry Sheehy[1,2]
[1] School of Physical Sciences, University of Kent, Canterbury CT2 7NH, United Kingdom
[2] QuantaLumin
(Dated: June 29, 2026)

We study a superconducting two-dimensional extension of the Su–Schrieffer–Heeger model in which a finite impurity wall is used as a tunable internal boundary. The clean model is a stack of momentum-resolved SSH chains; after imposing an inter-sublattice pairing field it supports Majorana-arc boundary modes in the same symmetry setting as the Weyl-SSH construction [1]. A one-cell-thick onsite potential wall is grown inside a periodic torus, with wall length ℓ and strength V controlling the promotion of a soft defect into a hard internal boundary. In the imposed-pairing problem, tracking the same wall-projected Bogoliubov-de Gennes branch by eigenvector overlap shows that the lowest positive bulk-like excitation at $k_y = 0$ is continuously promoted into a wall-local hard-wall-descendant branch as the scalar wall becomes strong. We define a normalized branch-promotion diagnostic $\eta_{\rm hw}(V)$ from this tracked branch and use it to characterize this soft-wall-to-boundary promotion. Across simulated device sizes, the onset remains diagnostic- and size-dependent, so we interpret it as finite-device branch promotion rather than as a thermodynamic transition. We then relax the pairing field with a self-consistent mean-field calculation. The wall does not simply scatter quasiparticles: it suppresses the local Gor'kov field and expels $|\Delta_{AB}|$ from the wall while leaving the off-wall condensate finite. The combined result is a controlled finite-device route from clean momentum-space topology to a real-space, tunable boundary in a microscopic superconducting SSH lattice.

I. INTRODUCTION

The one-dimensional SSH model is the canonical example of a chiral topological band problem with boundary zero modes [2]. Its two-dimensional extensions are useful because each transverse momentum can behave as a separate SSH chain, so the boundary spectrum records how a family of one-dimensional invariants evolves through momentum space [3–5]. When such a system is paired, the Bogoliubov-de Gennes (BdG) problem can host Majorana boundary arcs connecting projected Weyl nodes [1, 6–11]. Related Weyl-system superconductors show how pairing can split normal-state Weyl nodes into Bogoliubov-Weyl nodes and edge arcs [12–14].

This paper studies whether a local impurity wall inside a periodic superconducting SSH system can be tuned into an effective internal boundary carrying the arc physics. The finite-device setting begins as a torus, the wall is a microscopic perturbation, and increasing the wall strength promotes it toward a cut. The central result is that the wall strength controls the promotion of the lowest positive bulk-like $k_y = 0$ excitation into the near-zero hard-wall-descendant branch. Self-consistency changes the interpretation but not the basic picture: the wall also suppresses the anomalous field, so a strong wall is a boundary in the mean-field texture as well as in the single-particle Hamiltonian.

II. MODEL

We use spinless fermions on a square lattice of unit cells $r = (x, y)$, with two orbitals or sublattices A and B in each cell. The normal-state Hamiltonian is

$$\begin{aligned} H_0 = & -\sum_r \left[v\, c_r^{A\dagger} c_r^B + w\, c_r^{A\dagger} c_{r-\hat{x}}^B + \text{h.c.} \right] \\ & - \sum_{r,s=\pm 1} \left[t_d\, c_r^{B\dagger} c_{r+s\hat{y}}^A - t_d\, c_r^{B\dagger} c_{r+\hat{x}+s\hat{y}}^A + \text{h.c.} \right] \\ & + \sum_{r,\alpha=A,B} (\epsilon^\alpha - \mu) n_r^\alpha. \end{aligned} \tag{1}$$

For a translation-invariant torus this becomes

$$H_0(\boldsymbol{k}) = -\boldsymbol{h}(\boldsymbol{k}) \cdot \boldsymbol{\sigma} + (\bar{\epsilon} - \mu)\sigma_0, \tag{2}$$

with

$$h_x = v_1(k_y) + w_1(k_y) \cos k_x, \tag{3}$$
$$h_y = w_1(k_y) \sin k_x, \tag{4}$$
$$h_z = \delta\epsilon, \tag{5}$$

where $v_1(k_y) = v + 2t_d \cos k_y$, $w_1(k_y) = w + 2t_d \cos k_y$, $\bar{\epsilon} = (\epsilon^A + \epsilon^B)/2$, and $\delta\epsilon = (\epsilon^B - \epsilon^A)/2$.

The imposed-pairing BdG problem uses an onsite inter-sublattice pair field within each unit cell [15],

$$H_\Delta = \sum_{x,y} \left[\Delta_0 c_{x,y}^A c_{x,y}^B + \Delta_0^* c_{x,y}^{B\dagger} c_{x,y}^{A\dagger} \right], \tag{6}$$

written in the Nambu basis $\Psi_{\boldsymbol{k}} = (c_{\boldsymbol{k}}^A, c_{\boldsymbol{k}}^B, c_{-\boldsymbol{k}}^{A\dagger}, c_{-\boldsymbol{k}}^{B\dagger})^T$. We add the wall potential

$$H_V = V \sum_{(x,y)\in W_\ell} \sum_{\alpha=A,B} n_{x,y}^\alpha, \tag{7}$$

where W_ℓ is a one-cell-thick support of length ℓ. All real-space figures use centered unit-cell coordinates, so the plotted wall is at the center of the unit-cell coordinate system. Unless stated otherwise, real-space densities are cell-resolved sums over the A and B sites in each unit cell; pairing-field plots show the inter-sublattice cell field $|\Delta_{AB}(r)|$. The numerical conventions used in the production figures are collected in Table I. Additional reimplementation details for the branch tracker, wall projector, SCMFT iteration, and cached data are given in the Supplemental Material. Figure 1 shows this internal-wall geometry using a smaller representative torus.

III. CLEAN TOPOLOGICAL SLICES

For $\delta\epsilon = 0$, each fixed k_y slice is a chiral one-dimensional SSH Hamiltonian along x. The off-diagonal block is

$$q(k_x; k_y) = v_1(k_y) + w_1(k_y)e^{-ik_x}, \tag{8}$$

and the slice winding is

$$\nu(k_y) = \frac{1}{2\pi}\Delta_{k_x} \arg q(k_x; k_y). \tag{9}$$

Thus $\nu(k_y) = 1$ when $|w_1(k_y)| > |v_1(k_y)|$ and zero otherwise. The Weyl-SSH construction is the statement that the gap closings between these slices become the endpoints of boundary arcs after pairing [1]. In this language, the stacked SSH model supplies a k_y-dependent one-dimensional winding number; inter-sublattice spinless pairing becomes an effective p-wave gap after projection onto the winding Weyl bands; forced zeros of that projected gap intersect the Fermi pockets to create Bogoliubov-Weyl/Majorana nodes; and the change of the fixed-k_y one-dimensional BdG invariant across those nodes produces Majorana arcs on an edge. Previous Weyl-SSH studies characterized the clean/open-edge spectra and interaction-driven superconducting variants [1, 16, 17]; here the new ingredient is an impurity wall grown inside a periodic system. Figures 2 and 3 provide the clean-model reference: they identify the slice invariant and endpoint interval against which the internal-wall spectra are compared.

IV. FIXED-PAIRING SOFT-WALL PROMOTION

The imposed-Δ_0 calculation isolates the quasiparticle boundary problem. We use the fixed pairing amplitude $\Delta_0 = 0.3$ and first set $\mu = \delta\epsilon = 0$. For representative wall strengths, the wall-projected spectral function $A(k_y, E)$ shows the lowest positive bulk-like $k_y = 0$ excitation acquire wall weight and approach the near-zero hard-wall arc. The clean-model figures above define the endpoint interval; the following figures supply the finite-device evidence for branch promotion. The viewer-exported panels in Fig. 4 include a visible ADOS-ridge overlay, making the branch promotion visible at the scale of the printed figure. A broader wall-length and wall-strength atlas is shown in Fig. 5; it provides the phase-diagram-like visual overview, while the branch-continuation analysis below supplies the quantitative diagnostic. Unlike the open-edge spectra and wavefunction classification of the clean Weyl-SSH problem [1], these spectra are computed for an internal scalar wall in a periodic torus. The wall-projected spectral function plotted below is

$$A(k_y, E) = \sum_{n>0} P^{(n)}_{\text{wall}}(k_y)\frac{\eta_A/\pi}{[E - E_n(k_y)]^2 + \eta_A^2}, \tag{10}$$

where $P^{(n)}_{\text{wall}}$ is the norm of the BdG eigenvector on the wall projector, the sum is over positive-energy BdG states, and $\eta_A = 0.08$. For the finite-width wall projector we use a two-cell-wide strip around the impurity support with a two-cell pad along the wall direction; this choice is used only to visualize and track wall-local spectral weight, not to change the Hamiltonian.

To quantify this promotion, we label the branch by hard-wall ancestry rather than selecting a new local minimum at each parameter point. For each sampled k_y, the production tracker diagonalizes the BdG Hamiltonian on the wall-strength grid in Table I. It first seeds the target state at $V_{\max} = 100$ by selecting the positive-energy wall-supported state in the projected Weyl interval. It then steps downward in V and chooses the state with maximum eigenvector overlap with the previously selected state. At near-degeneracies, it also compares overlap with the nearby-state subspace used to represent the hard-wall descendant; steps with a small single-vector overlap gap are flagged as ambiguous in the checkpoint metadata. The resulting branch is the red curve in Fig. 6. This method turns the hard-wall-descendant branch into a reproducible object, distinct from a purely visual ridge fit to $A(k_y, E)$. The same branch definition is used in all finite-size checks below. We regard a thermodynamic transition as established only if this branch produces a size-stable order-parameter collapse, a consistent finite onset V_c, and a matching quasiparticle-gap diagnostic that closes at the same scale. If these requirements are not met, the proper interpretation is finite-device branch promotion rather than a thermodynamic transition.

The $k_y = 0$ point of this tracked branch provides a normalized diagnostic for the wall-driven branch promotion. Let $\epsilon_{\text{arc}}(0; V)$ be the wall-projected ADOS branch energy at $k_y = 0$, i.e., the distance from $E = 0$ to the selected positive-energy peak. We define

$$\eta_{\text{hw}}(V) = \frac{|\epsilon_{\text{arc}}(0; V) - \epsilon_{\text{arc}}(0; V_{\min})|}{|\epsilon_{\text{arc}}(0; V_{\max}) - \epsilon_{\text{arc}}(0; V_{\min})|}. \tag{11}$$

For the production tracker $V_{\min} = 0.1$ and $V_{\max} = 100$; $V_{\min}$ is used as the weak-wall numerical reference because it lies on the same continuation grid as the large-V branch tracker. The resulting $\eta_{\text{hw}}(V)$ rises from zero to one as the tracked branch moves from its weak-wall bulk-like value toward its strong-wall hard-wall-descendant value.

TABLE I. Numerical parameters and conventions used in the production figures. All energies are in units of the hopping scale used in Eq. (1), and the lattice spacing is set to one. The fixed-pairing and SCMFT calculations use the same hopping parameters but different sublattice offset in the SCMFT checkpoint set, as stated below.

Quantity	Value	Usage
v, w, t_d	$0.6, 1.2, 0.9$	SSH hopping parameters in Eq. (1)
Boundary condition	periodic in x, y	internal wall on a torus
Main real-space size	$L_x = L_y = 41$	spectra, tracking, LDOS, SCMFT
Fixed-pairing fields	$\Delta_0 = 0.3$, $\mu = 0$, $\delta\epsilon = 0$	imposed-BdG spectra and tracking
Fixed-pairing atlas	$\ell = 1, 5, 19, 41$; $V = 0, 2, 5, 10, 1000$	publication subset of cached grid
Tracked branch grid	$\ell = 41$; $V = 0.1, 0.2, 0.5, 1, \ldots, 100$; 241 k_y points	Fig. 7, Table II
Spectral broadening	$\eta_A = 0.08$	Lorentzian broadening in $A(k_y, E)$
SCMFT fields	$g_{AB} = 2.9249$, $\mu = 0$, $\delta\epsilon = 0.1$	relaxed-field checkpoint set
SCMFT iteration	$\eta_{\rm mix} = 0.35$, 80 iterations	fixed-point residuals in Table III
SCMFT interpolation	$\lambda = 0, 0.5, 1$; $V = 0, 2, 5, 10$	Fig. 11
Finite-size audit	$L = 21, 31, 41, 51, 61, 71, 81, 91, 101, 121, 141$	Appendix A

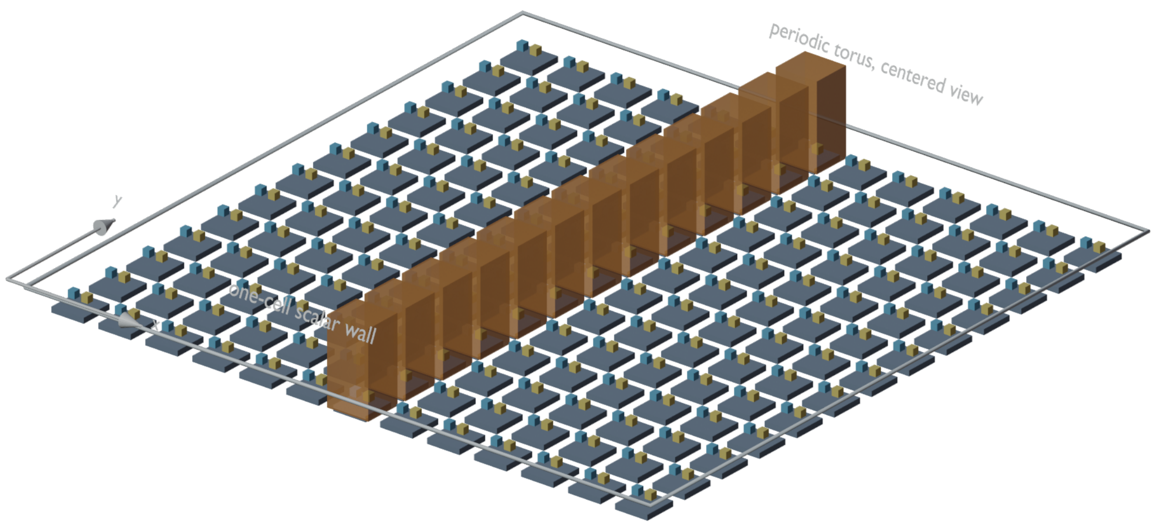

FIG. 1. Three-dimensional view of the periodic wall setup used in the numerical calculations. The orange cells mark the one-cell-thick scalar wall, the small blue and gold blocks show the two sublattice sites in each unit cell, and the compact axes indicate the centered real-space coordinates used throughout the paper. The transparent render emphasizes that the wall is an internal defect on a periodic torus rather than an imposed open edge. The render uses a 13×13 representative lattice for clarity; the main fixed-pairing spectra and real-space diagnostics below use 41×41 unit cells unless stated otherwise.

The largest jump in the 41×41 full-wall data occurs between $V = 2.5$ and $V = 3$, which we identify as the finite-device onset window. This onset marks where the lowest positive bulk-like excitation at $k_y = 0$ is promoted into a wall-local hard-wall-descendant branch. The physical intent of $\eta_{\rm hw}$ is to measure the descent and localization of that wall-enhanced $k_y = 0$ candidate, not to define an order parameter. We therefore also define a branch-character diagnostic from the hard-wall reference-subspace overlap,

$$\Omega_{\rm hw}(V, L) = \frac{P_{\rm hw}(V, L) - P_{\rm hw}(0, L)}{P_{\rm hw}(V_{\max}, L) - P_{\rm hw}(0, L)}, \qquad (12)$$

where $P_{\rm hw}$ is the projection of the tracked $k_y = 0$ state onto the large-V hard-wall descendant subspace. This quantity measures change in hard-wall ancestry rather than only the energy height. The $L = 21, 31, 41, 51, 61, 71, 81, 91, 101, 121, 141$ eigenvector-

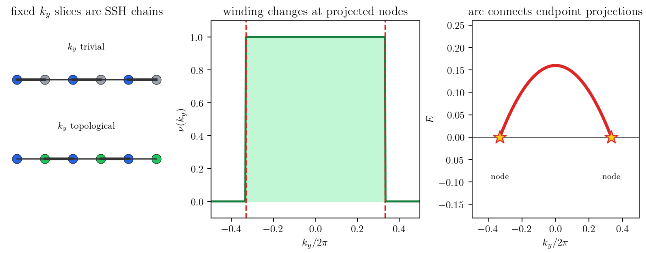

FIG. 2. Clean-model reference for the Weyl/Majorana arc mechanism. Fixed k_y slices are SSH chains along x. The winding changes across the projected Weyl nodes, and the paired boundary spectrum carries an arc connecting the endpoint projections. This cartoon motivates the endpoint interval; it is not the evidence for wall-induced branch promotion, which is supplied by the internal-wall spectra and eigenvector tracking below.

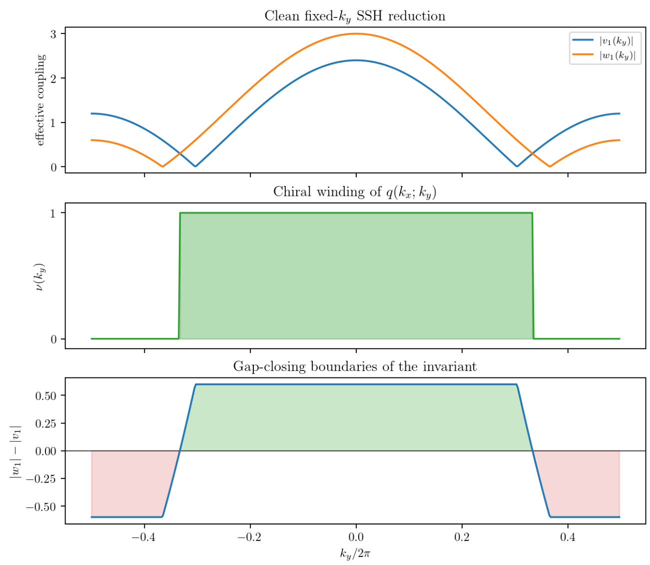

FIG. 3. Clean bulk slice topology used as a reference calibration. For $\delta\epsilon = 0$, each k_y slice reduces to a chiral SSH chain along x. The winding changes when the effective intracell and intercell hoppings exchange magnitude. This clean slice invariant fixes where the open-boundary Majorana arc should begin and end. The impurity-wall calculations below then test, by spectra, branch tracking, and localization, whether an internal scalar wall reproduces that boundary response.

continuation run shows a decreasing tracked-branch gap proxy with size, but the branch-character onset and gap estimates are not mutually size-stable. We therefore use the 41×41 wall-strength scan as a finite-device branch-promotion diagnostic and collect the supporting consistency checks in Appendix A.

The same branch promotion is visible in real space. The LDOS and component-resolved wavefunction diagnostics in Fig. 8 show the wall-normal localization of selected spectral contributions and the signed BdG amplitudes for the strong-wall near-zero mode. Together these

TABLE II. Representative fixed-Δ_0 branch-continuation output for the full-wall 41×41 calculation. $\epsilon_{\rm arc}(0;V)$ is the tracked positive branch energy at $k_y = 0$, and $\eta_{\rm hw}$ is normalized by Eq. (11) with $V_{\min} = 0.1$ and $V_{\max} = 100$.

V	$\epsilon_{\rm arc}(0;V)$	$\eta_{\rm hw}(V)$
0.1	0.5289	0.000
1.0	0.5226	0.013
2.0	0.5066	0.044
2.5	0.4969	0.063
3.0	0.2831	0.486
5.0	0.2573	0.537
10.0	0.1890	0.672
100.0	0.0232	1.000

localization diagnostics confirm that the tracked spectral branch is not merely a relabelled bulk eigenvalue. In the BdG basis $\Psi = (c_A, c_B, c_A^\dagger, c_B^\dagger)^T$, a wall eigenstate has spinor $\psi = (u_A, u_B, v_A, v_B)^T$. Particle-hole symmetry pairs the state at energy E with a partner at $-E$; at an exact Majorana zero mode the spinor can be gauge-fixed so that $v_\alpha = e^{i\phi} u_\alpha^*$. The strong-wall state in Fig. 8 is therefore read as Majorana-like when the tracked branch approaches this particle-hole self-conjugate limit while remaining on the arc connecting the projected Weyl-node endpoints.

V. SELF-CONSISTENT WALL FEEDBACK

We now let the anomalous field respond to the wall by solving a self-consistent inter-sublattice pairing problem, following the real-space BdG mean-field strategy used for inhomogeneous topological superconductors [15, 18]. The interaction is decoupled through the Gor'kov field

$$\kappa_{AB}(r) = \langle c_r^A c_r^B \rangle, \tag{13}$$

with the local mean-field order parameter

$$\Delta_{AB}(r) = g_{AB}\kappa_{AB}(r). \tag{14}$$

Here $\kappa_{AB}(r)$ and $\Delta_{AB}(r)$ are local inter-sublattice cell fields. The plots show $|\Delta_{AB}(r)|$, or averages of this magnitude over wall and off-wall cell sets, so the displayed quantity is insensitive to the global sign convention for the real pairing gauge used in the calculation. This self-consistent field is distinct from the imposed constant Δ_0 used in the fixed-pairing BdG problem. The production calculation uses $g_{AB} = 2.9249$ and $\delta\epsilon = 0.1$, chosen so the clean off-wall pairing amplitude is comparable to the imposed $\Delta_0 = 0.3$ reference while avoiding a numerically marginal relaxed-field checkpoint. The fixed-point iteration uses linear mixing,

$$\Delta_{AB}^{(n+1)} = (1-\eta)\Delta_{AB}^{(n)} + \eta\, \Delta_{AB}^{\text{new},(n)}, \tag{15}$$

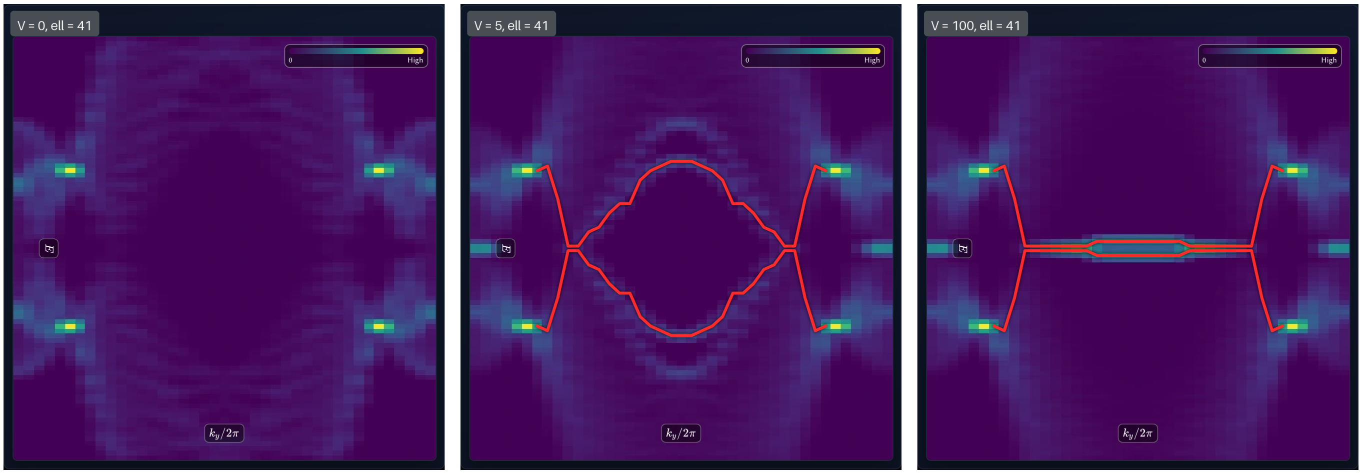

FIG. 4. Viewer-exported wall-strength spectra for the imposed-pairing model on 41×41 unit cells. The panels show $A(k_y, E)$ at $\Delta_0 = 0.3$, $\mu = \delta\epsilon = 0$, $\ell = 41$, and $V = 0, 5, 100$. The red curve follows the visible ADOS ridge and is clipped to the projected Weyl-node interval $|k_y|/2\pi \leq 1/3$. It is a visual ridge overlay; the separate continuation diagnostic in Fig. 7 records the eigenvector-tracking and ambiguity checks. At weak V, the wall-projected spectrum resembles the bulk response. At intermediate V, the selected branch starts to acquire wall character and move below the bulk-scale response. At strong V, the wall acts as an internal hard boundary and the near-zero arc is visible.

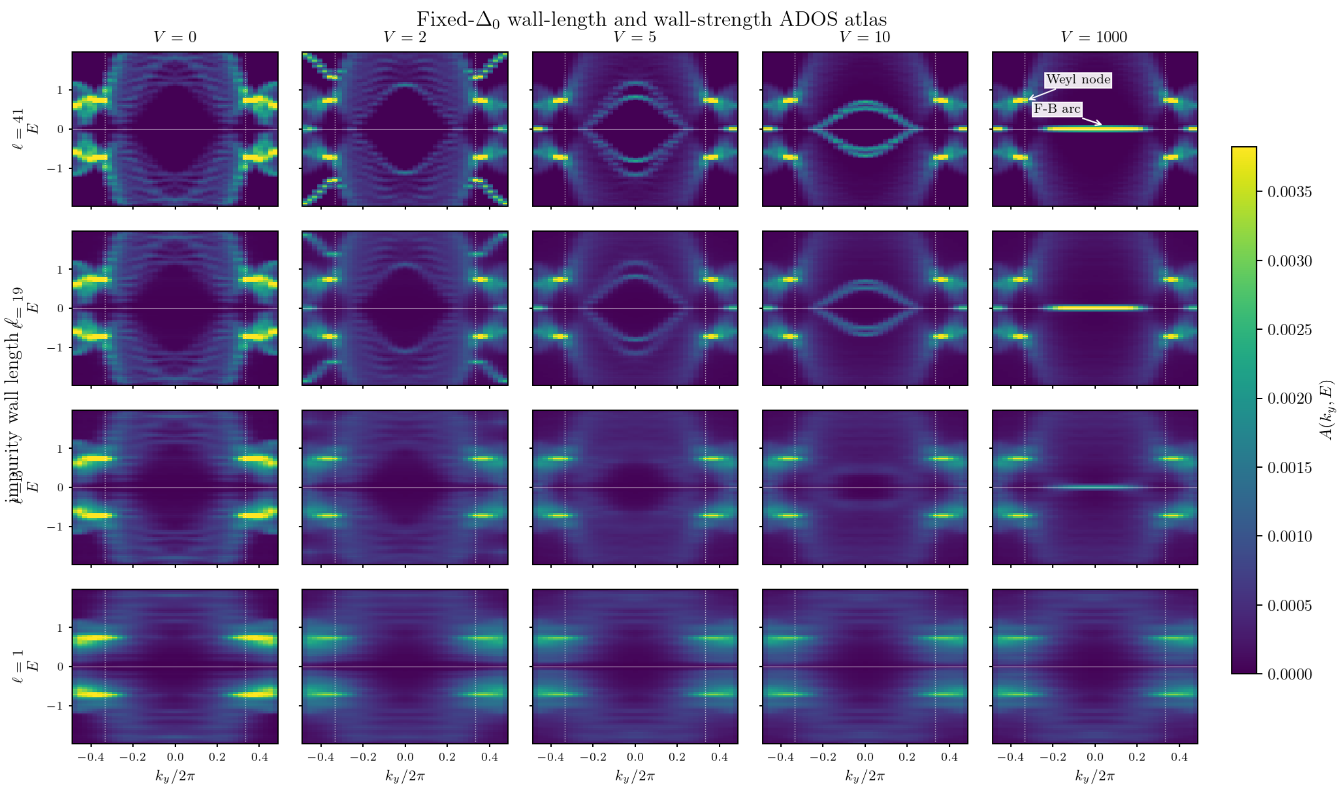

FIG. 5. Wall-length and wall-strength atlas for the imposed-pairing soft-wall problem. Each small panel shows the wall-projected spectral function $A(k_y, E)$ on the 41×41 torus, with $\Delta_0 = 0.3$, $\mu = 0$, and $\delta\epsilon = 0$. This publication subset uses $V = 0, 2, 5, 10, 1000$ and $\ell = 1, 5, 19, 41$ to show the progression from a single impurity to a full internal partition, and from weak to hard-wall strength. The full cached grid, including intermediate values of V and ℓ, is retained in the accompanying code. The dotted vertical lines mark the projected Weyl-node momenta. Short walls do not define a sharp transverse boundary channel, so their wall-projected spectra are intrinsically broader than the full-partition spectra. The figure is a visual ADOS overview: it shows how the Fermi-Bogoliubov arc becomes apparent as the wall becomes long and strong, but it does not by itself define the branch identity or a transition criterion. The quantitative branch label used in the rest of the paper is the eigenvector-continuation diagnostic in Fig. 7.

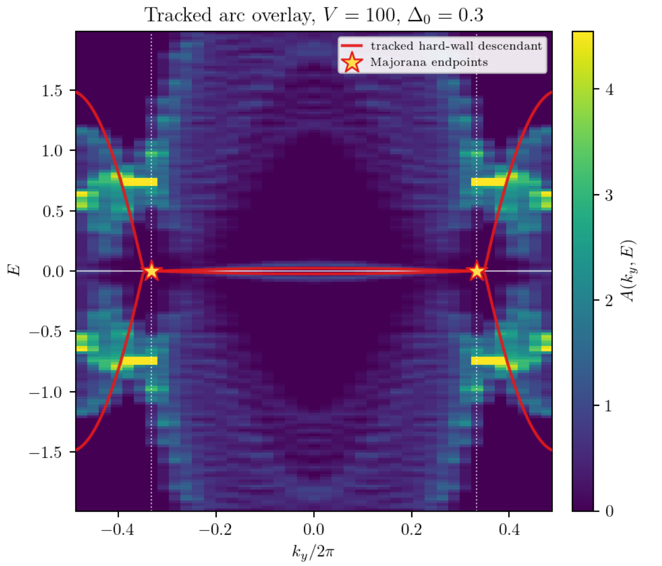

FIG. 6. Tracked Weyl arc on top of the wall-projected spectrum. The background is $A(k_y, E)$. The red curve is the hard-wall-descendant BdG branch selected by eigenvector and nearby-subspace overlap, and the yellow stars mark the clean Majorana endpoints at $k_y/2\pi = \pm 1/3$. Open yellow circles, when present, mark continuation steps flagged as branch-identity ambiguous by the overlap-gap diagnostic. The line representation is important: the calculation follows one continuous hard-wall-ancestry branch rather than plotting unrelated spectral maxima or the brightest ADOS ridge at each k_y.

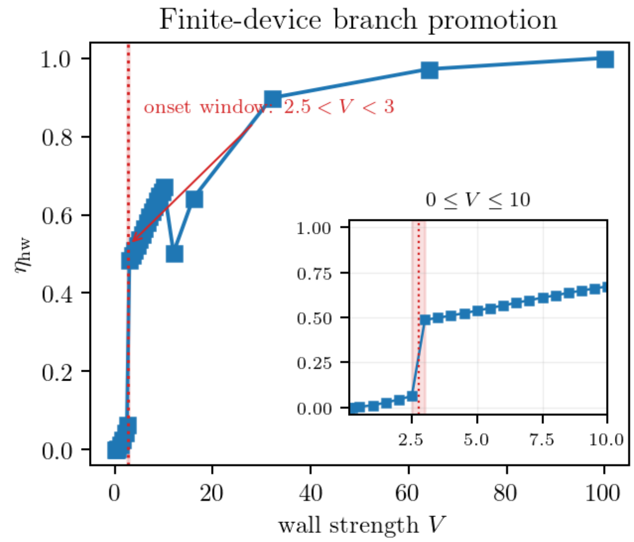

FIG. 7. Fixed-Δ_0 branch-promotion diagnostic. The panel shows the normalized full-wall diagnostic $\eta_{\rm hw}(V)$ from Eq. (11). The data use a full wall on a 41×41 unit-cell device with $\Delta_0 = 0.3$ and are obtained by eigenvector continuation, not by following the visible ADOS-ridge overlay used in the viewer-exported spectra. The branch is the lowest positive bulk-like excitation at weak impurity strength and is promoted toward a wall-local near-zero hard-wall descendant as the wall becomes strong. The shaded band marks the finite-size onset window $2.5 < V < 3$. This window is not treated as a fitted transition point; it is the wall strength range over which the finite device promotes the selected bulk-like excitation into the hard-wall-descendant branch.

where η is the weight of the new update. The reported production checkpoints use $\eta = 0.35$ for 80 iterations; Table III reports the final fixed-point residual rather than assuming exact convergence.

The self-consistent calculation shows that the wall is not only a scattering potential for quasiparticles. It also creates a local depression of the anomalous field: $|\Delta_{AB}(r)|$ is strongly suppressed on the wall support while the off-wall condensate remains finite. Table III summarizes the main self-consistent amplitudes. The wall mean falls by more than an order of magnitude over the simulated range, while the off-wall mean remains close to the clean scale. Attempts to fit the wall mean to the same finite-V_c ansatz as the fixed-Δ_0 arc are unstable. A simpler interpretation is that SCMFT replaces the sharp imposed-Hamiltonian branch promotion by an algebraic depletion tail, $|\Delta_{AB}|_{\rm wall} \sim (V - V_0)^{-\beta}$ with β of order unity over the simulated interval. This is a separate physical effect: the boundary condition is now partly generated by the suppression of the anomalous field itself. Figure 9 compares the imposed and self-consistent wall profiles directly. Figure 10 then repeats the wall-normal LDOS and BdG-component diagnostic using the tuned self-consistent field. Figure 11 shows the corresponding spectral deformation when the BdG Hamiltonian is rebuilt from fields interpolating between the imposed reference and the relaxed SCMFT texture. Across this interpolation, the wall-projected ADOS is not qualitatively reorganized: self-consistency mainly depletes and reshapes the local pairing amplitude, while the visible arc-like spectral structure remains controlled primarily by the scalar wall. This supports using the fixed-Δ_0 atlas as the clean branch-promotion diagnostic, with SCMFT providing a feedback and robustness check rather than a separate mechanism. The full convergence and field-map scan is shown in Appendix A, Fig. 13.

VI. DISCUSSION

The fixed-Δ_0 and SCMFT calculations tell complementary parts of the same story. In the fixed-pairing model, the Hamiltonian is controlled enough that one can track a BdG eigenbranch through k_y and measure a finite-device diagnostic for the soft-wall-to-boundary promotion. This is the cleanest statement of the Weyl-arc result: at $k_y = 0$, the lowest positive bulk-like excitation is continuously promoted into a wall-local near-zero hard-wall-descendant branch as V grows.

In the self-consistent model, the wall has an additional channel. It suppresses $\kappa_{AB}(r)$ and therefore $\Delta_{AB}(r)$ on

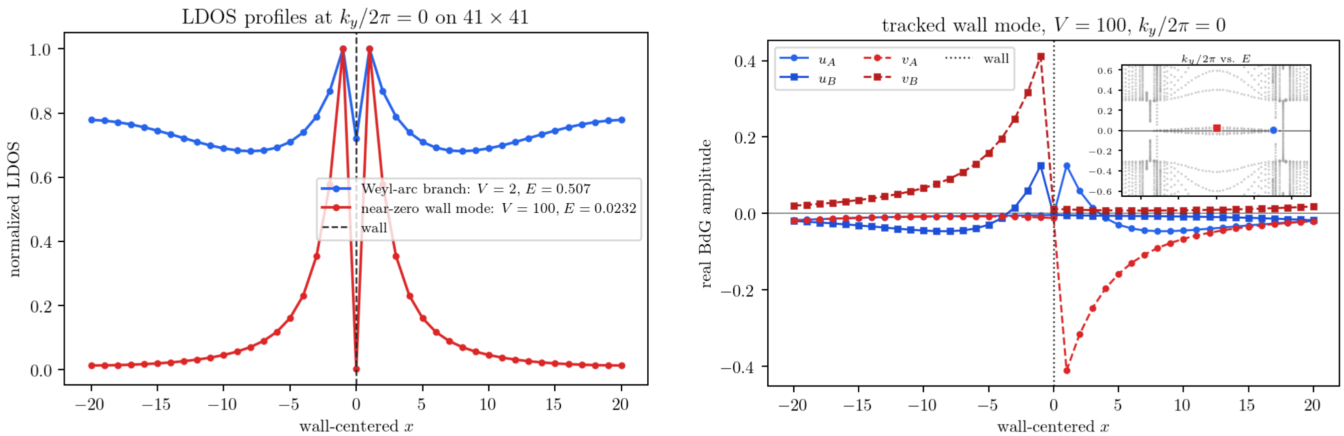

FIG. 8. Real-space localization and spinor structure of the wall modes on 41×41 unit cells. Left: wall-normal LDOS profiles at $k_y/2\pi = 0$. The Weyl-arc branch uses $V = 2$ and $E = 0.507$, while the near-zero wall mode uses $V = 100$ and $E = 0.0232$. Each LDOS curve is normalized by its own maximum so the comparison emphasizes wall-normal localization, and the wall is marked at $x = 0$. Right: component-resolved BdG wavefunction of the tracked strong-wall mode at $V = 100$, $k_y/2\pi = 0$, and $E = 0.0232$. The curves show the real amplitudes (u_A, u_B, v_A, v_B) versus wall-centered x. The global phase is fixed by making the largest component real and positive, so the signs are a gauge-fixed diagnostic of the mode structure. The inset shows a subsampled strong-wall strip spectrum versus $k_y/2\pi$; the red square marks the near-zero Majorana point used in the main panel and the blue circle marks a representative point on the same tracked Bogoliubov-Fermi arc. This panel adapts the standard Majorana spinor check to the impurity-wall eigenstate rather than repeating the clean open-edge result.

TABLE III. Self-consistent pairing amplitudes for the wall-stability scan. The wall mean is the average of $|\Delta_{AB}(r)|$ on the impurity support; the off-wall mean excludes the support. The residual is the final fixed-point residual after the fixed 80-iteration run.

V	$\lvert\Delta_{AB}\rvert_{\mathrm{wall}}$	$\lvert\Delta_{AB}\rvert_{\mathrm{bulk}}$	residual
0.0	0.318	0.318	5.59×10^{-4}
1.0	0.318	0.331	1.76×10^{-4}
1.2	0.139	0.326	5.47×10^{-4}
1.5	0.0480	0.321	1.32×10^{-4}
2.0	0.0271	0.327	2.49×10^{-4}
3.0	0.0150	0.337	3.94×10^{-4}
5.0	0.00649	0.346	3.25×10^{-4}
10.0	0.00147	0.355	1.07×10^{-4}
100.0	3.33×10^{-6}	0.363	7.36×10^{-5}
1000.0	1.97×10^{-8}	0.363	9.07×10^{-6}

the wall support, while the off-wall condensate remains finite. This means that the wall is not just a probe of a pre-existing BdG spectrum. It changes the mean-field problem itself by creating a narrow region where the anomalous field is expelled. The resulting behavior is better described as wall-local depletion with an algebraic tail, and the evidence supports a finite-device branch-promotion interpretation rather than a finite-V_c phase-transition ansatz.

Because the wall is an onsite scalar potential, it is not an ideal chiral-symmetric cut. The result should therefore be read as impurity-induced boundary formation in a finite BdG device, not as a quantized inhomogeneous AIII invariant.

The conclusion is that a finite impurity wall in a two-dimensional superconducting SSH lattice can be promoted into an effective internal boundary. The evidence is a linked chain: clean slice winding, slab Majorana arcs, wall-projected spectral evolution, eigenvector-continuous arc tracking, real-space mode localization, and a self-consistent suppression of the wall pairing field. What remains for a sharper claim is a fully quantized real-space invariant for the inhomogeneous BdG wall, in the spirit of defect and class-D real-space invariant frameworks [19, 20], or an explicit disorder and size-scaling analysis showing that the tracked arc and SCMFT depletion survive outside the current finite-device regime. The completed large-size and branch-aware checks support the narrower interpretation used here: the observed onset is finite-device promotion of a bulk-like branch into a wall-local hard-wall descendant.

ACKNOWLEDGMENTS

An early version of this work was presented at ExoSup 2022, the Cargèse Summer School on Exotic Superconductivity. I thank Jorge Quintanilla for suggesting the problem and for encouraging me to continue pursuing it. Numerical data and figures were generated with the `qulab.research.ssh_2d` module in QuLab [21].

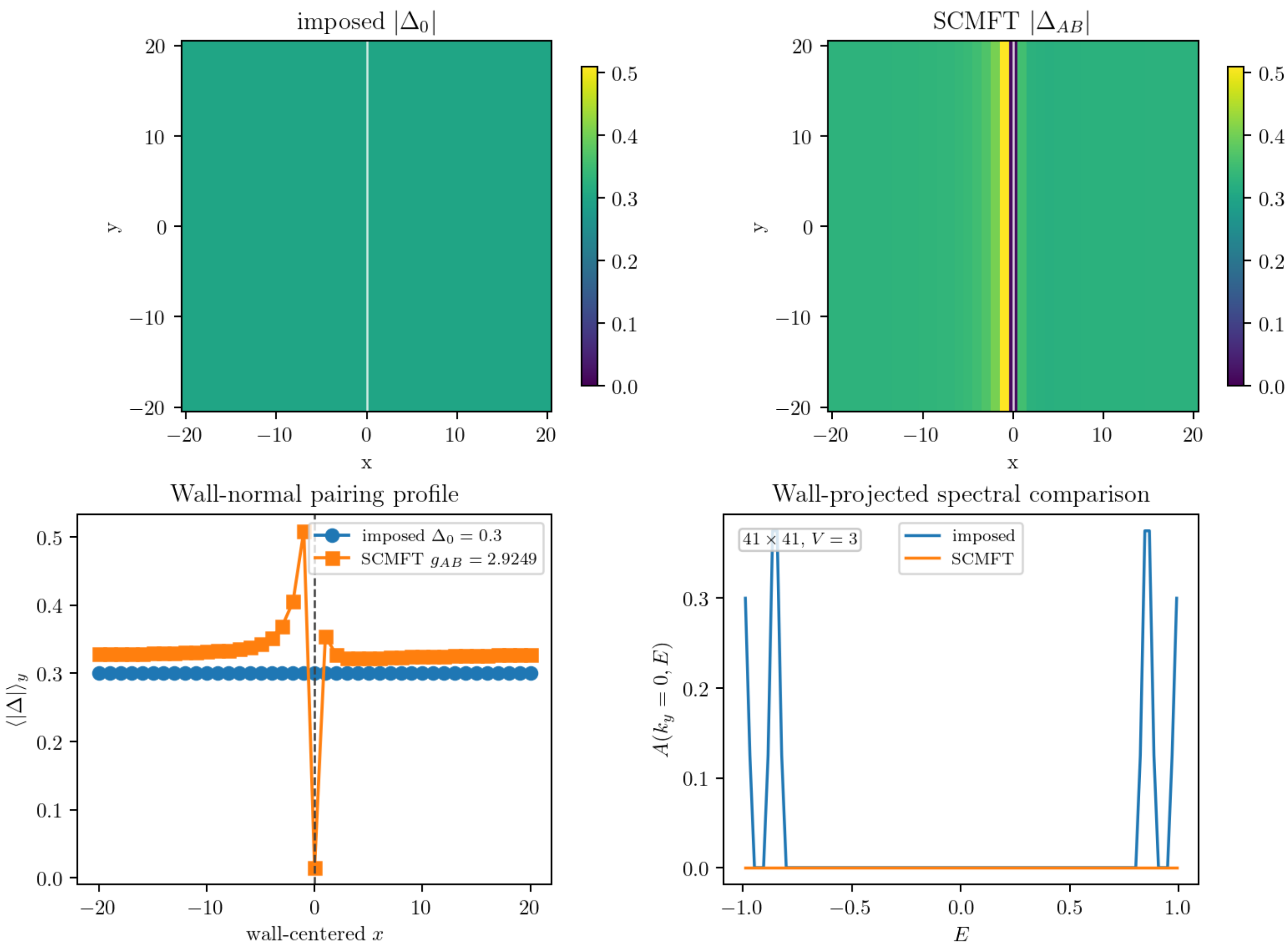

FIG. 9. Direct fixed-pairing versus SCMFT comparison at the same wall. The imposed calculation keeps $|\Delta_0|$ uniform, while the SCMFT solution suppresses the local $|\Delta_{AB}(r)|$ at the wall and leaves the off-wall condensate finite. Thus the self-consistent wall does not merely scatter quasiparticles; it also depletes the local anomalous field.

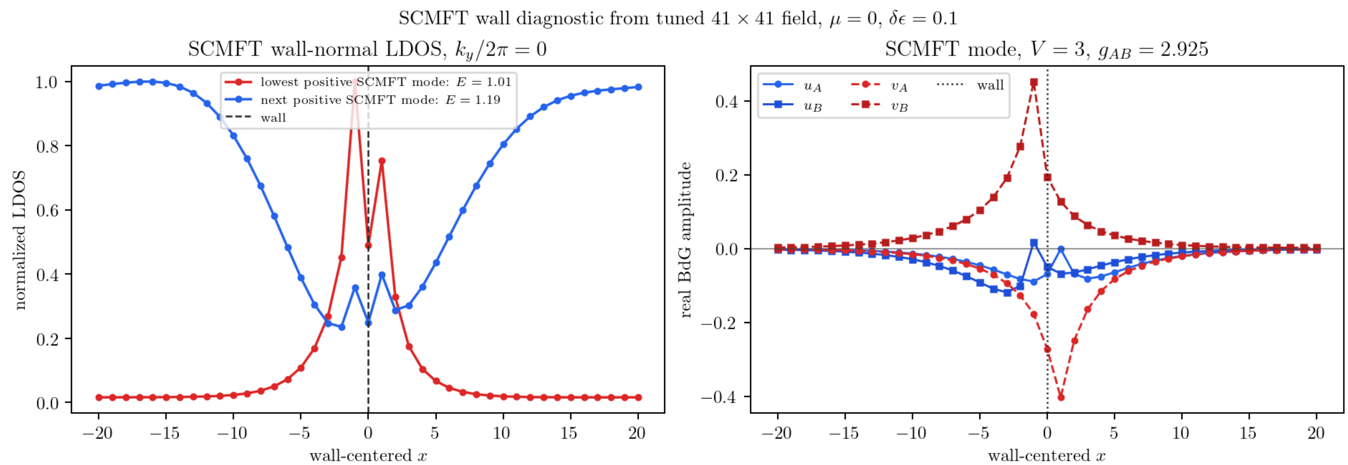

FIG. 10. SCMFT wall-normal mode diagnostic constructed from the tuned 41×41 self-consistent field. The calculation uses the converged wall-normal average of $\Delta_{AB}(r)$ from the $g_{AB} = 2.9249$, $V = 3$ SCMFT checkpoint and diagonalizes the corresponding $k_y = 0$ wall-normal strip. Left: normalized LDOS profiles for the two lowest positive SCMFT strip modes. Right: gauge-fixed real BdG components (u_A, u_B, v_A, v_B) for the lowest positive mode. Compared with the fixed-Δ_0 diagnostic in Fig. 8, the relaxed SCMFT field does not simply reproduce the imposed hard-wall near-zero mode; it gives a wall-localized positive branch on top of a pairing texture that is strongly depleted at the wall. This is an interpretation diagnostic of the relaxed field, not the primary ground-state or finite-size-scaling evidence.

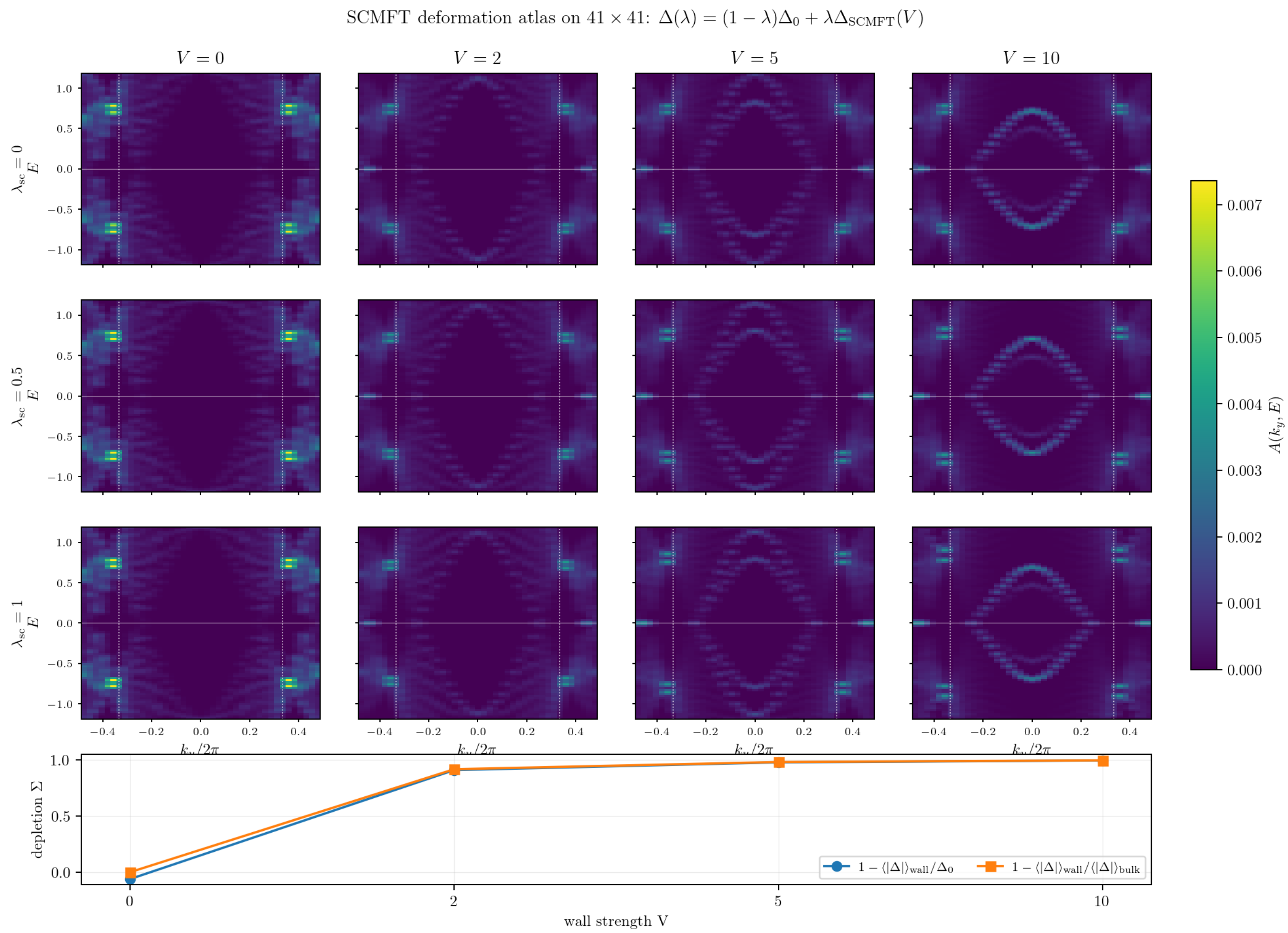

FIG. 11. SCMFT deformation atlas for the wall-projected spectrum on the 41 × 41 torus. Each panel shows $A(k_y, E)$ after rebuilding the BdG Hamiltonian with $\Delta_{AB}^{(\lambda)}(r) = (1-\lambda)\Delta_0 + \lambda\Delta_{AB}^{\mathrm{SCMFT}}(r;V)$. Thus $\lambda = 0$ is the fixed-Δ_0 reference for the same wall strength, while $\lambda = 1$ uses the fully relaxed SCMFT field from the checkpoint calculation. This publication subset uses full-partition SCMFT checkpoints at $V = 0, 2, 5, 10$, and the rows use $\lambda = 0, 0.5, 1$. The full cached grid, including the omitted wall strengths $V = 1$, $V = 100$, and $V = 1000$, is retained in the accompanying code. The bottom panel records the corresponding depletion measures of the relaxed field. The comparison shows that the relaxed pairing texture changes amplitudes and spectral weights more than it changes the qualitative ADOS morphology. This figure is a spectral diagnostic of self-consistent wall feedback; it is complementary to the fixed-Δ_0 wall-length atlas in Fig. 5, not a replacement for the branch-continuation evidence.

Appendix A: Additional diagnostics

This appendix collects supporting diagnostic figures that check finite-size consistency and self-consistent convergence without interrupting the main spectral narrative.

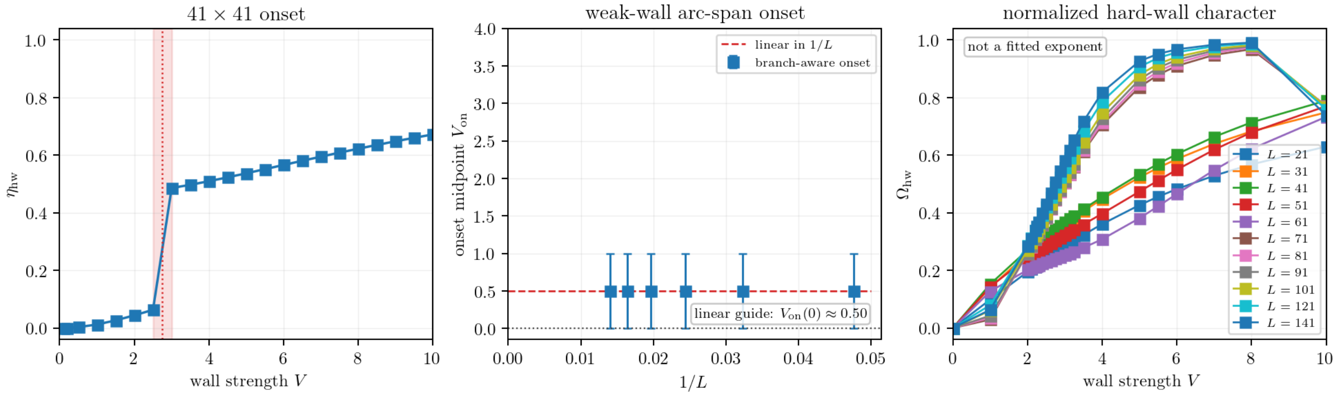

FIG. 12. Finite-size consistency checks for the branch-promotion onset. Left: the 41×41 branch-promotion diagnostic $\eta_{hw}(V)$ has its largest jump between $V = 2.5$ and $V = 3$ in the ADOS/eigenvalue diagnostic. Middle: the branch-aware emergence onset is plotted versus $1/L$ for $L = 31, 41, 51, 61, 71$. This arc-span proxy turns on at weak wall strength and does not isolate a positive common V_c. Right: the normalized hard-wall-character diagnostic $\Omega_{hw}(V, L)$ is shown for the $L = 21, 31, 41, 51, 61, 71, 81, 91, 101, 121, 141$ descendant-tracking run. The tracked-branch gap proxy decreases with size, but the Ω_{hw} collapse is not stable, tail-window gap fits do not establish a zero intercept, and the onset definitions are not mutually consistent. These tests support the finite-device branch-promotion interpretation and do not supply a stable thermodynamic transition criterion.

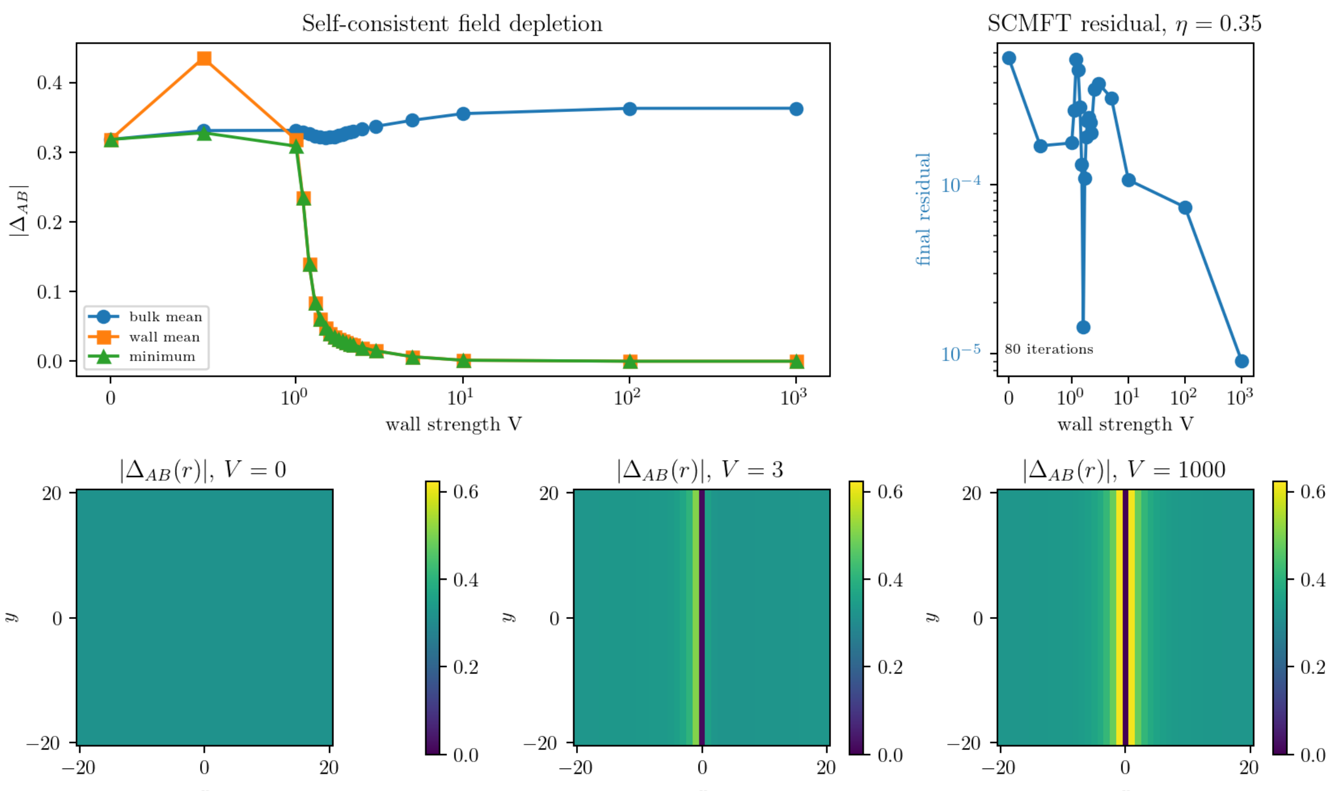

FIG. 13. Self-consistent mean-field wall response. The upper panels track the bulk mean, wall mean, and minimum of $|\Delta_{AB}(r)|$ together with the final SCMFT residual. The lower panels show representative real-space inter-sublattice field maps at zero, intermediate, and strong wall strength. The wall is not only a quasiparticle scatterer: it suppresses the local Gor'kov field and expels the pairing amplitude from the wall support. The off-wall condensate remains finite, while the wall-local field decreases rapidly with V.

[1] P. Rosenberg and E. Manousakis, Topological superconductivity in a two-dimensional weyl ssh model, Physical Review B **106**, 054511 (2022), arXiv:2203.12004 [cond-mat.supr-con].

[2] W. P. Su, J. R. Schrieffer, and A. J. Heeger, Solitons in polyacetylene, Physical Review Letters **42**, 1698 (1979).

[3] B.-H. Chen, *Two-Dimensional Extended Su–Schrieffer–Heeger Model*, Master's thesis, National Taiwan Normal University (2018).

[4] C.-A. Li, Topological states in two-dimensional su-schrieffer-heeger models, Frontiers in Physics **10**, 861242 (2022).

[5] P. M. Tam, J. W. F. Venderbos, and C. L. Kane, Topology of nonsymmorphic two-dimensional su-schrieffer-heeger models, Physical Review B **105**, 045106 (2022).

[6] A. P. Schnyder, S. Ryu, A. Furusaki, and A. W. W. Ludwig, Classification of topological insulators and superconductors in three spatial dimensions, Physical Review B **78**, 195125 (2008).

[7] S. Ryu, A. P. Schnyder, A. Furusaki, and A. W. W. Ludwig, Topological insulators and superconductors: tenfold way and dimensional hierarchy, New Journal of Physics **12**, 065010 (2010).

[8] A. Y. Kitaev, Unpaired majorana fermions in quantum wires, Physics-Uspekhi **44**, 131 (2001).

[9] N. Read and D. Green, Paired states of fermions in two dimensions with breaking of parity and time-reversal symmetries and the fractional quantum hall effect, Physical Review B **61**, 10267 (2000).

[10] C. Nayak, S. H. Simon, A. Stern, M. Freedman, and S. Das Sarma, Non-abelian anyons and topological quantum computation, Reviews of Modern Physics **80**, 1083 (2008).

[11] J. Alicea, New directions in the pursuit of majorana fermions in solid state systems, Reports on Progress in Physics **75**, 076501 (2012).

[12] T. Meng and L. Balents, Weyl superconductors, Physical Review B **86**, 054504 (2012).

[13] G. Bednik, A. A. Zyuzin, and A. A. Burkov, Superconductivity in weyl metals, Physical Review B **92**, 035153 (2015).

[14] Z. Faraei and S. A. Jafari, Induced superconductivity in weyl semimetals, Physical Review B **100**, 035447 (2019).

[15] J.-X. Zhu, *Bogoliubov-de Gennes Method and Its Applications*, Lecture Notes in Physics, Vol. 924 (Springer, Cham, 2016).

[16] P. Rosenberg, N. Aryal, and E. Manousakis, Numerically exact study of weyl superconductivity, Physical Review B **100**, 104522 (2019).

[17] P. Rosenberg and E. Manousakis, Weyl nodal-ring semimetallic behavior and topological superconductivity in crystalline forms of su-schrieffer-heeger chains, Physical Review B **104**, 134511 (2021).

[18] M. Hori, T. Sugimoto, T. Tohyama, and K. Tanaka, Self-consistent study of topological superconductivity in two-dimensional quasicrystals, Physical Review B **110**, 144512 (2024).

[19] J. C. Y. Teo and C. L. Kane, Topological defects and gapless modes in insulators and superconductors, Physical Review B **82**, 115120 (2010).

[20] M. Rodriguez-Vega, T. A. Loring, and A. Cerjan, Dimensional crossover of class d real-space topological invariants, Communications Physics **8**, 480 (2025).

[21] H. Sheehy, Qulab research module for two-dimensional ssh soft walls (2026), repository module: qulab.research.ssh_2d.